Comparing High-Resolution Snow Mapping Approaches in Palsa Mires: UAS LiDAR vs. Modeling

Alexander Störmer[1,3], Timo Kumpula[2,3], Miguel Villoslada[2,3,4], Pasi Korpelainen[2,3],
Henning Schumacher[1,3], and Benjamin Burkhard[1,3]

[1]Institute of Earth System Sciences, Physical Geography and Landscape Ecology, Leibniz University Hannover, Hannover, 30167, Germany
[2]Department of Geographical and Historical Studies, University of Eastern Finland, Joensuu, 80101, Finland
[3]Kilpisjärvi Biological Station, University of Helsinki, Kilpisjärvi, 99490, Finland
[4]Institute of Agriculture and Environmental Sciences, Estonian University of Life Sciences, Tartu, Estonia

Correspondence to: Alexander Störmer (stoermer@phygeo.uni-hannover.de)

Abstract. Snow cover has an important role in permafrost processes and dynamics, creating cooling and warming systems, impacting the aggradation and degradation of frozen soil. Despite theoretical, experimental, and remote sensing-based research, comprehensive understanding of small-scaled snow distribution at palsas remains limited. ~~This study~~~~compares two approaches to generate spatially continuous, small-scale snow distribution models in palsa mires in northwestern Finland based on Digital Surface Models: a machine learning approach using the Random Forest (RF) algorithm with~~ *in-situ* ~~measured snow depth data and an~~ In this study, we used Unmanned Aerial System (UAS) equipped with ~~a~~ Light Detection and Ranging (LiDAR) ~~sensor~~to generate high-resolution Digital Terrain Models (DTMs) and derive spatially continuous snow depth maps over palsa mires in northwestern Finland. For the first time, snow distribution was recorded over a palsa using UAS LiDAR~~data. The aim is to review which approach is more accurate overall and which snow distribution patterns can be identified. In comparison~~. The resulting snow depth maps showed sufficient accuracy, with a root mean square error (RMSE) of 23.49 cm and an R^2 value of 0.691 when compared to *in-situ* ~~collected validation data, both the RF results and UAS LiDAR data show sufficient~~ measured snow depth validation data. To enhance the interpretation of snow distribution patterns, we applied a Random Forest (RF) machine learning model trained with *in-situ* snow depth measurements and terrain parameters derived from the UAS LiDAR DTMs. This approach resulted in improved accuracy, with ~~a~~ an RMSE of 18.33 cm ~~(RF) and 23.49 cm (LiDAR) and~~ and an R^2 value of 0.77~~respectively 0.691~~. RF performs particularly well in modeling snow distribution over ~~open water~~ thermokarst and vegetated areas, demonstrating the potential of machine learning to capture small-scale patterns based on field observations. The UAS LiDAR also enables a very detailed analysis of the interactions between snow and permafrost. Both approaches reveal snow accumulation zones, especially at steep palsa margins and within cracks, where insulation limits frost penetration and contributes to degradation processes such as block erosion. In contrast, a thinner snow depth on exposed palsa surfaces allows deeper frost penetration, which initially stabilizes the ice core but leads to the formation of steep edges and further degradation.

1   Introduction

Snow cover plays an important role in permafrost processes and dynamics. Its physical characteristics impact the aggradation and degradation of frozen soil (Barry, 2002). In March 2023, around 39.26 million km^2 of the ~~northern hemisphere~~ Northern Hemisphere were permanently or partly covered ~~by~~ with snow (NOAA, 2023), affecting around 14.77 million km^2 permafrost area (Ran et al., 2022). This includes the discontinuous permafrost areas in northern parts of Sweden, Norway and Finland, known as Fennoscandia. Due to changes in climate, a reduction in snow cover duration is expected (Quante et al., 2021), leading to changes of air and soil temperature interactions and resulting in negative impacts for permafrost soils (Chen et al., 2021). This has a direct impact on ecological processes, such as a reduced albedo in winter that leads to a higher energy uptake by soils (Thackeray and Fletcher, 2016) and longer growing seasons (Madani et al., 2023). In addition, Wang et al. (2024) showed that snow cover – in combination with landscape heterogeneity - plays an important role in controlling soil temperatures throughout the year. The Intergovernmental Panel on Climate Change (IPCC) already highlighted in their latest report that a loss of permafrost within this century is expected in these regions (IPCC, 2023). In northern Fennoscandia, particularly in northern Finnish Lapland - the main focus of this study - specific periglacial permafrost landforms known as palsas are at risk of disappearing within this century (Leppiniemi et al., 2023).

The occurrence of palsas, small mounds up to 4 - 7 m height with a frozen core, is bound mainly to the presence of peatlands and driven by climatic parameters (Meier, 2015; Seppälä, 2011). Palsas serve as indicators of climate warming, as their degradation and disappearance reflect rising temperatures (Leppiniemi et al., 2023). Additionally, they provide important habitats for various animal species (Luoto et al., 2004) and hold significant cultural and societal value for indigenous and local communities, particularly in the context of traditional reindeer herding (Markkula et al., 2019). Given their ecological and cultural importance, monitoring their changes is essential. Palsas are highly sensitive to temperature insulation shifts induced by snow during winter. Their development is directly influenced by variations in snow depth, which regulate thermal insulation in winter and protect against warm air and sunlight in spring, ultimately affecting Active Layer Thickness (ALT) and soil warming (Park et al., 2015; Verdonen et al., 2023, 2024). In winter, deep snow cover insulates the ground, reducing the penetration of cold temperatures and keeping the underlying soil comparatively warmer. In summer, this accumulated snow delays ground warming and slows permafrost thawing, resulting in a shallower ALT. These areas are defined as warming areas throughout this article. They are typically found in depressions, concave terrain, or wind-sheltered locations where snowdrifts accumulate. Conversely, thin snow cover allows for more intensive winter cooling due to reduced insulation, leading to greater heat loss from the ground. In summer, these areas warm up earlier, causing a deeper ALT. Such locations are defined as cooling areas. They are commonly found in elevated or wind-exposed areas of the palsa, where snow accumulation is naturally limited (Seppälä, 1982; Olvmo et al., 2020). This influence on palsas has been empirically demonstrated by Seppälä (2011), who described the impact of variable snow cover on palsa thermal dynamics during subsequent thawing periods. Moreover, experiments show that mainly the depth of snow cover influences the development of palsas (Seppälä, 1982). Deviations from the usual thickness of snow cover, whether thinner or thicker, induce varying conditions for palsa dynamics. For example, at the steep edges of palsas, the accumulation of snow can pose a risk by destabilizing the frozen core due to increased thermal insulation at

these specific areas leading to a higher risk of block erosion (Olvmo et al., 2020; Seppälä, 1994). Despite theoretical, experimental, and remote sensing-based research, comprehensive understanding of actual snow distribution conditions within and around palsas remains limited (Seppälä, 2011; Verdonen et al., 2023). Although they have high potential for accurate mapping, Unmanned Aerial Systems (UAS) have not yet been used to measure snow depth in palsa mires.

Consequently, detailed data on snow distribution in palsa mires is not available. Even if sufficient climate data is made available through official weather stations, it is the microclimate inside these mires that impacts the snow distribution in various ways, especially by snow drifts due to strong winds, as monitored by Zuidhoff (2002). Since palsa mires occur mostly in remote areas, simple interpolation of climatic observations from weather stations within the same region does not provide data on the actual state within these mire complexes, which does not allow ~~to monitor~~ monitoring the exact snow distribution (Verdonen et al., 2023). Only *in-situ* measured snow depth data can provide clear insights into these conditions. However, to date and to our knowledge, no small-scale mapping of snow depth in palsa mires has yet been carried out.

Measuring snow depth manually demands a relatively high workload in time and effort under mostly harsh climatic conditions. Thus, measurements of snow depth over a long time span without technical help have been undertaken in Finnish Lapland by only a few researchers, e.g. by Leppänen et al. (2016), who describe the snow survey program by the Finnish Meteorological Institute (FMI) that was established in 1909 in Sodankylä. Statistical evaluations of collected data at weather stations were published for whole Finnish Lapland (Merkouriadi et al., 2017).

The use of remote sensing data and methods to monitor snow depth has become increasingly important in snow research. Optical and radar satellite data have been widely utilized to map snow distribution (Marti et al., 2016; Hu et al., 2023), but their coarse resolution limits their effectiveness, particularly in capturing small-scale variations in ground surface conditions. Small-scale structures, such as palsas, exhibit substantial snow depth heterogeneity, making satellite-derived datasets unsuitable for analyzing these localized processes. To improve spatial resolution, UAS RGB-derived photogrammetry has been increasingly used for high-resolution snow depth mapping. With small grid sizes (10 cm × 10 cm or 5 cm × 5 cm), these methods provide detailed snow depth estimates. Bühler et al. (2016) and Michele et al. (2016) successfully applied this approach to directly map snow depth in alpine terrain, while Rauhala et al. (2023) and Meriö et al. (2023) evaluated the accuracy of UAS RGB surveys in Finnish Lapland, showing that they can produce spatially representative snow depth estimates. However, RGB-derived approaches face challenges in capturing the ground surface, particularly in environments with dense vegetation as suggested by Walker et al. (2021), who explored the accuracy of UAS RGB-derived snow depth mapping and suggested that an approach that better filters out vegetation could improve the mapping results. Recently, UAS equipped with Light Detection and Ranging (LiDAR) sensors have been introduced as an alternative for snow depth monitoring. Unlike RGB sensors, which passively capture optical images, LiDAR actively emits laser pulses and measures their return time to generate high-resolution, three-dimensional surface models. Harder et al. (2020) demonstrated that LiDAR can accurately capture vegetation, allowing for its removal from ground surface data, which significantly improves snow depth estimation. Similarly, Jacobs et al. (2021) showed that ~~LiDAR-based~~ LiDAR-derived vegetation filtering enhances snow cover mapping in forestry and open areas. Given the limitations of satellite data in resolving small-scale snow depth variations and the challenges of RGB-based photogrammetry

in vegetated terrain, we employ UAS LiDAR to generate high-resolution snow depth models. Its ability to capture vegetation and provide precise elevation data makes it particularly suitable for monitoring snow depth in subarctic permafrost landscapes. Another method to estimate snow distribution is the application of statistical machine learning models like the *Random Forest* (RF) algorithm (Breiman, 2001). RF is a widely used method of ensemble learning that is characterized by complex, non-linear relationships between predictor variables and is therefore suitable for environmental modeling. In snow research, RF has been used primarily for large-scale mapping of snow distribution in mountainous regions (Meloche et al., 2022; Revuelto et al., 2020; Richiardi et al., 2023), where it has demonstrated good predictive capabilities through the integration of remote sensing, topographic and meteorological data. However, these studies mainly focused on coarser spatial scales with resolutions of more than 1 m × 1 m, which limits their applicability for analyzing small-scale snow distribution patterns. To our knowledge, RF has not yet been systematically applied to high-resolution snow depth modeling in subarctic and permafrost environments, such as Finnish Lapland. As small-scale variations in snow depth play a crucial role in permafrost dynamics, investigating the feasibility of RF for such detailed applications could provide valuable insights for future research and monitoring needs.

In this study, we compare and evaluate two methods for generating high-resolution snow distribution maps at three exemplary palsa sites in northernmost Finland: (i) snow depth derived from UAS LiDAR data and (ii) snow depth simulated using a~an RF modeling approach. *In-situ* measured snow depth data was~is used to train the RF model as well as to validate the results obtained with both methods. The primary objective of this study is to assess the accuracy and suitability of these methods for small-scale snow distribution mapping. Specifically, we investigate whether RF can effectively model small-scale snow depth patterns, providing a cost-effective alternative to UAS LiDAR methods. In addition, we investigate the spatial distribution of snow depth at palsas and their surroundings based on the results of the methods to identify characteristic small-scale variation patterns. The results provide a basis for discussing relationships between snow distribution and palsa dynamics. To address these objectives, we focus on the following research questions: (1) How accurately can UAS LiDAR and RF modeling estimate snow depth, and which approach provides the most reliable results, and (2) and how do the snow depth patterns derived from UAS LiDAR and RF modeling compare, and what does this reveal about small-scale snow distribution?

2 Study sites

The palsa sites under investigation - Puolikkoniva, Pousu and Peera - are located ca. 30 km south from the closest Finnish Meteorological Institute's (FMI) weather station in Kilpisjärvi, Finland (Fig. 1). These sites are located along the Könkämäeno river, a significant terrain depression with numerous palsas, and are adjacent to the region's primary main road (European Route E8) in the northwestern part of Finnish Lapland (Fig. 1 (a, b)). While Peera has been previously described by Verdonen et al. (2023), Pousu and Puolikkoniva were not yet investigated.
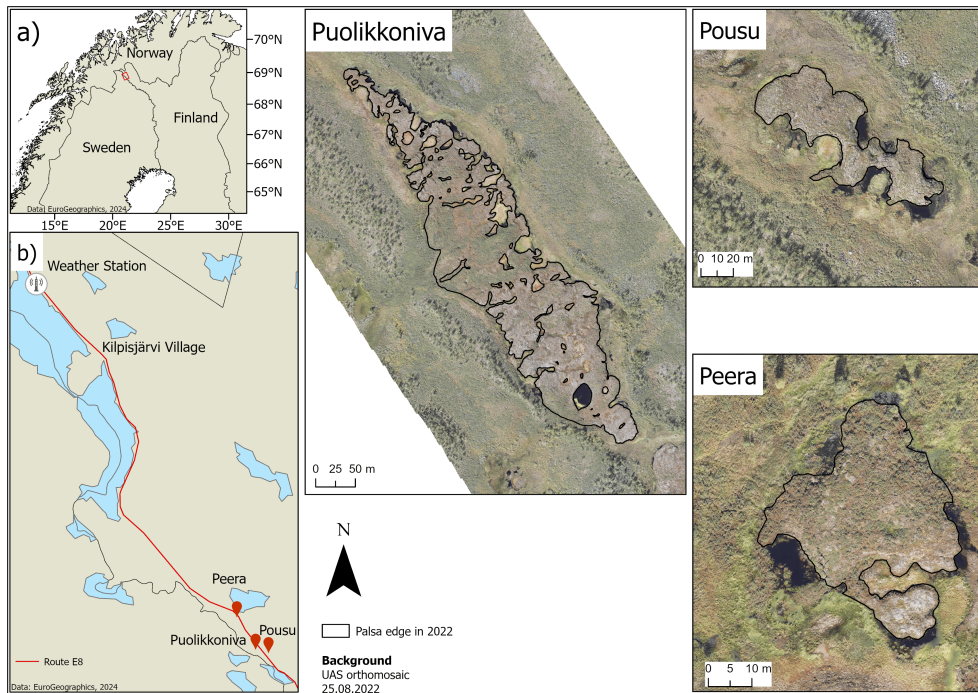
Figure 1. Location of the study sites Puolikkoniva, Pousu and Peera in north-western Finland (a). Climate data used in this study are from the Kilpisjärvi weather station, from which the distance to the palsa sites is around 20 km (b). Basemaps obtained from EuroGeographics (2024).

2.1 Palsa mire sites
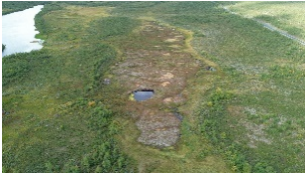
Puolikkoniva is located approximately 2.3 km south of lake Peerajärvi at 68°51'43" N, 21°06'18" E and around 455 m a.s.l, surrounded at the eastern part by the Könkämäeno river and ~~in~~ extends to the west by the main road. The study site has an area of roughly 4.26 ha, with a maximum height difference to the surrounding peatland of ca. 2 m. This palsa is about 590 m in length and 130 m in width. Puolikkoniva is a prototypical longitudinal plateau palsa, consisting of several single and complex shaped palsas. According to the definition of Seppälä (2006) and Meier (2015), the palsas contain a perennially frozen core of peat with segregated ice. Numerous cracks traverse the palsa site, with dwarf shrubs (5 - 20 cm high, e.g. *Rubus chamaemorus, Empetrum hermaphroditum*) and dwarf birches (5 - 60 cm high, *Betula nana*) at the edges, while atop and around the palsas, typical vegetation such as lichens (up to 3 cm high, e.g. *Cetraria spp., Cladonia spp.*) and sphagnum mosses (under 3 cm high, e.g. *Sphagnum lindbergii*) dominates. The absence of distinct dome-shaped structures and the presence of thermokarst ponds within the palsa structure indicate the degradation of the palsa (Seppälä, 2011), with pronounced block erosion at steep edges.

Pousu is located approximately 600 m east of the Puolikkoniva palsa at 68°51'39" N, 21°07'17" E and around 470 m a.s.l, 150 m east of the main road. This study site covers an area of about 0.36 ha and has a maximum height difference to the surrounding peatland of ca. 2.5 m. This site, measuring 130 m in length and 50 m in width, is a classic example of a degrading

dome-shaped palsa, as shown by collapsed parts, block erosion at its steep edges and thermokarst ponds within the former palsa structure. Similar to Puolikkoniva, typical palsa mire vegetation grows around and on it.

Peera is located at 68°52'45" N, 21°04'35" E and around 460 m a.s.l., approximately 400 m south of lake Peerajärvi and 100 m west of the main road. This study site encompasses an area of about 0.13 ha and has a maximum height difference to the surrounding peatland of ca. 2 m. This palsa is about 55 m in length and 45 m in width. The palsa structure is surrounded by typical peatland vegetation such as sphagnum mosses and sedges. Water bodies, peat and bare rock structures can be found at the edges of the palsa. Mainly lichens and dwarf shrubs grow on top of the palsa. Similar to Pousu, this palsa is also dome-shaped and in a degrading phase. Verdonen et al. (2023) point out a significant decrease in the surface area of the palsa during the past 15 to 60 years.

Table 1. Main characteristics of each palsa site. Images recorded with DJI mini 3 Pro UAS at 30.08.2023.

	Puolikkoniva	Pousu	Peera
UAS image			
Location	68°51'43" N, 21°06'18" E	68°51'39" N, 21°07'17" E	68°52'45" N, 21°04'35" E
Area	4.26 ha	0.36 ha	0.13 ha
Extent (length, width)	590 m, 130 m	130 m, 50 m	55 m, 45 m
Height	2 m	2.5 m	2 m

2.2 Climate

The investigation areas are located on the pre-alpine belt of the Scandes. For the time period 1991 - 2020, the annual mean temperature is -1.30 °C, the annual mean precipitation amount is about 515 mm and the dominating wind direction is south-southeast from November to April (FMI, 2022). Higher mountains influence local weather conditions, e.g. clouds get held in front of mountains or wind directions are influenced (Autio and Heikkinen, 2002). This may lead to different precipitation amounts or wind directions and speeds than measured at the Kilpisjärvi weather station (Verdonen et al., 2023). Also, high wind speeds during winter can lead to a more intensive snow drift, influencing the snow distribution inside the mire sites (DeWalle and Rango, 2008).

The palsa mire sites are affected by cold winters and moderate warm summers (Fig. 2). Winter is the longest season, lasting about 200 days including the polar night, with around 50 days without sunlight. During winter, the temperature can drop close to - 50 °C and can increase above 0 °C (FMI, 2024). In Kilpisjärvi, the duration of permanent snow cover lasts about 217 days a year (Lépy and Pasanen, 2017). During spring, the snow cover melts away, and the growing season starts in late May. In late August the growing season ends with the beginning of autumn which lasts around 102 days (Kauhanen, 2013).
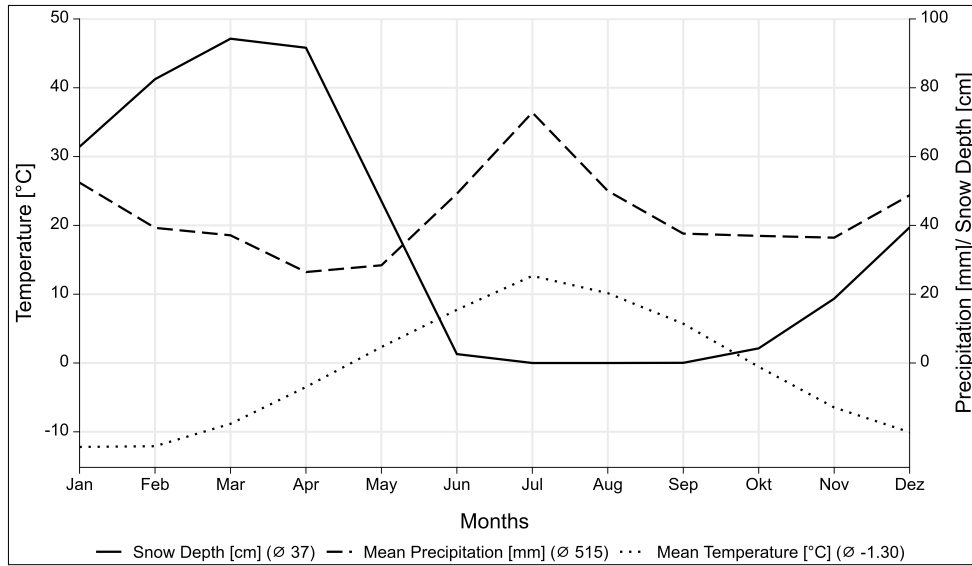
Figure 2. Climate chart of Kilpisjärvi (FMI, 2022). Climate data measured at 69.03905N, 20.81379E and 474 m.a.s.l. in the period 1991 - 2020. Dotted line shows 2 m above ground temperature in °C, dashed line shows precipitation in mm and solid line shows snow depth in cm. The *Köppen-Geiger* climate classification is Dfc.

3 Data and methods

In late August 2022 and late March 2023, field expeditions to the palsa mire sites were conducted to collect a comprehensive dataset consisting of UAS LiDAR data and *in-situ* snow depth measurements for modeling purposes. Late August was chosen specifically for the collection of summer data as it corresponds with the peak of the growing season and the maximum ALT, which typically occurs in this region by the end of August and mid-September, depending on annual weather patterns and the onset of frost (Verdonen et al., 2023). This timing ensures the capture of the landscape's conditions in its various states before the start of ~~the winterseason~~winter, providing the basis for extracting relevant input parameters for our approach. The input parameters are spatial datasets calculated on the basis of elevation data derived from UAS LiDAR.

On the contrary, late March was chosen for the ~~the~~ winter dataset based on historical climatological patterns in the Kilpisjärvi region, which typically have maximum snow depths at this time (FMI, 2024). This period allowed the collection of data under conditions that reflect winter extremes, which serves as both validation and training data for the RF modeling. Figure 3 shows an overview of the different steps carried out for this work.
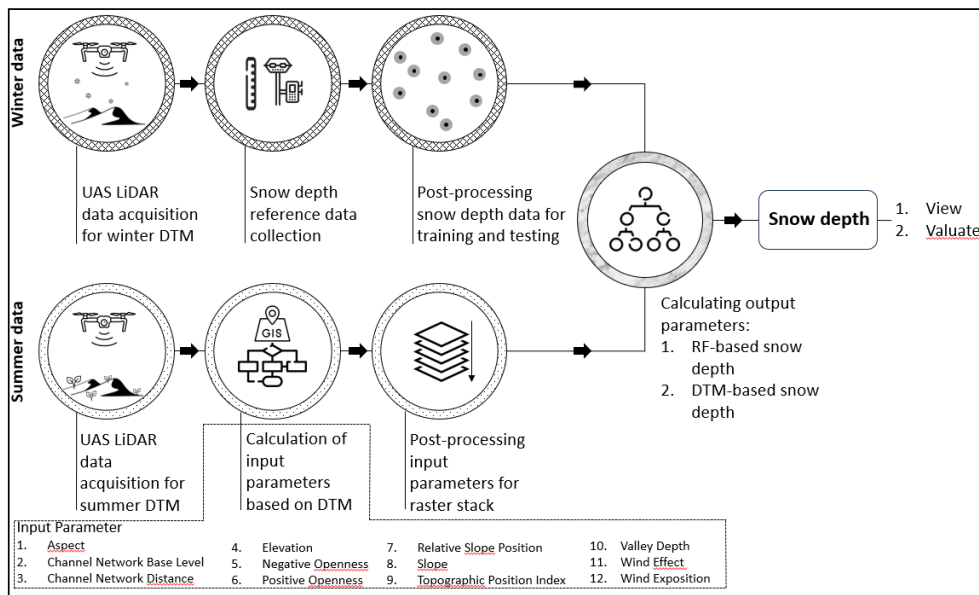
Figure 3. General overview of the data collection and analysis.

3.1 UAS Data

3.1.1 UAS data collection

For the initial collection of UAS LiDAR data to generate input parameters, aerial surveys were conducted at all three study sites on August 27, 2022, using a DJI Matrice 300 RTK, equipped with a YellowScan Mapper+ LiDAR system that scanned at a wavelength of 905 nm. The flight altitude was 30 m for each palsa, with a 50% side overlap. The flight direction was along the longitudinal axis of the palsas, except for Peera palsa, which followed an east-west orientation. The flight trajectories are pictured in Fig. 4. To improve the accuracy of the collected data, we used Ground Control Points (GCPs), measured with a Trimble R12i Real-Time Kinematic (RTK) GNSS. We have established several permanent GCPs located on known points of large stones in the study sites. Permanent GCPs have been established because we are monitoring changes in the palsas by collecting drone data annually since the past 8 years. The accuracy of these RTK GPS-measured GCPs is between 1–2 cm. For all UAS LiDAR summer flights we utilized these GCPs: three for Peera, 20 for Pousu, and 30 for Puolikkoniva.

The winter survey replicated the methodological framework of the summer survey, using the same drone and sensor. The flights for all three study sites were carried out on March 23 (Puolikkoniva and Pousu) and 24 (Peera), 2023. The flight altitude was 60 m, with a 50% side overlap. The flight direction was along the longitudinal axis of each palsa (see Fig. 4). For each side we used four GCPs, positioned around the palsa. The accuracy for each GCP is between 1 - 2 cm.

In addition, high-resolution RGB images were captured with an Autel EVO II Pro V2 to create an orthopicture in Agisoft Metashape Professional software of each palsa site during both surveys, enabling a comprehensive analysis of the site's condi-

tions. The flight altitude was 80 m, with a 75% side overlap for each flight. The RGB flights were conducted using the drone's internal RTK system.

3.1.2 UAS data post-processing

The acquired LiDAR data were post-processed using YellowScan CloudStation, resulting in point clouds for each flight. Mean point densities per square meter vary from 1064 (summer) to 831 (winter) for Peera site, 308 to 338 for Pousu site and 260 to 313 for Puolikkoniva site. To refine the flight trajectories, we used Receiver Independent Exchange Format (RINEX) data in the Position and Orientation System Post-processing software (POSPac). For each dataset, we obtained RINEX data from the continuously operating reference station (CORS) of the National Land Survey of Finland (NLS) in Kilpisjärvi (*KILP 2147250.4266 820562.0462 5930136.8831*).

For noise and vegetation removal in the dataset, we used the progressive Morphological Filter (PMF) described by (Zhang et al., 2003) and (Jacobs et al., 2021) in order to receive Digital Terrain Models (DTM). We applied the filtering using window sizes of 0.5, 1, 2 and 3 and thresholds of 0.05, 0.1, 0.3 and 0.5. The extracted ground points were saved in point cloud format. Using the software CloudCompare, we generated a DTM for each flight mission in 0.1 m x 0.1 m resolution with the *Rasterize* function. Empty cells within the point clouds were interpolated with a triangle max edge length value of 5.0.

Based on the summer and winter DTM of the palsa sites, snow distribution datasets were calculated by ~~substracting~~ subtracting the winter by the summer DTM in Geographic Information Systems (GIS) ~~-~~ using *ArcGIS Pro* by Esri~~was used -~~, allowing the comparison of UAS LiDAR conducted snow depth (SD_{LiDAR}) and RF modeled (SD_{RF}).

3.2 Reference data collection

Additional datasets that are essential for modeling and validation were collected after the respective flights. Snow depth measurements ($SD_{in\text{-}situ}$) were carried out manually using a wooden yardstick across all sites, whereas each point was measured at the snow cover surface by RTK GPS to receive the exact location. On March 23, 2023, $SD_{in\text{-}situ}$ were measured in Puolikkoniva and Pousu and on March 24, 2023, in Peera. A total of 185 validation points were recorded, divided across the sites as follows: 100 in Puolikkoniva, 46 in Pousu, and 39 in Peera (Fig. 4).

To ensure the derivation of a diverse $SD_{in\text{-}situ}$ training dataset, different measurement network designs were attempted at each site, customised to the unique geomorphological features of the palsa mires, making sure to catch points on top of the palsa, at the edges and at the steep slopes, on the thermokarst ponds and the surrounding field as at those parts differences in snow depth can be expected. In Pousu, a randomised sampling strategy was applied with focus on the palsa edges and summits (Fig. 4 b). In Puolikkoniva, there were two parallel transects measured following its longitude shape and complemented by randomised points at the edge, thermokarst and surrounding field (Fig. 4 a). The Peera approach consisted of two intersecting transects, augmented by a set of randomly chosen points along the edge (Fig. 4 c). This training dataset captures the variability of snow cover within palsa mires, ranging from snow-free palsa summits to deeply covered palsa edges, allowing a distribution of all $SD_{in\text{-}situ}$ into point classes *Edge*, *On Top*, *Open Area* and *Thermokarst*. A histogram of $SD_{in\text{-}situ}$ can be viewed in Appendix A1 and the distribution to the respective classes in Appendix A2.
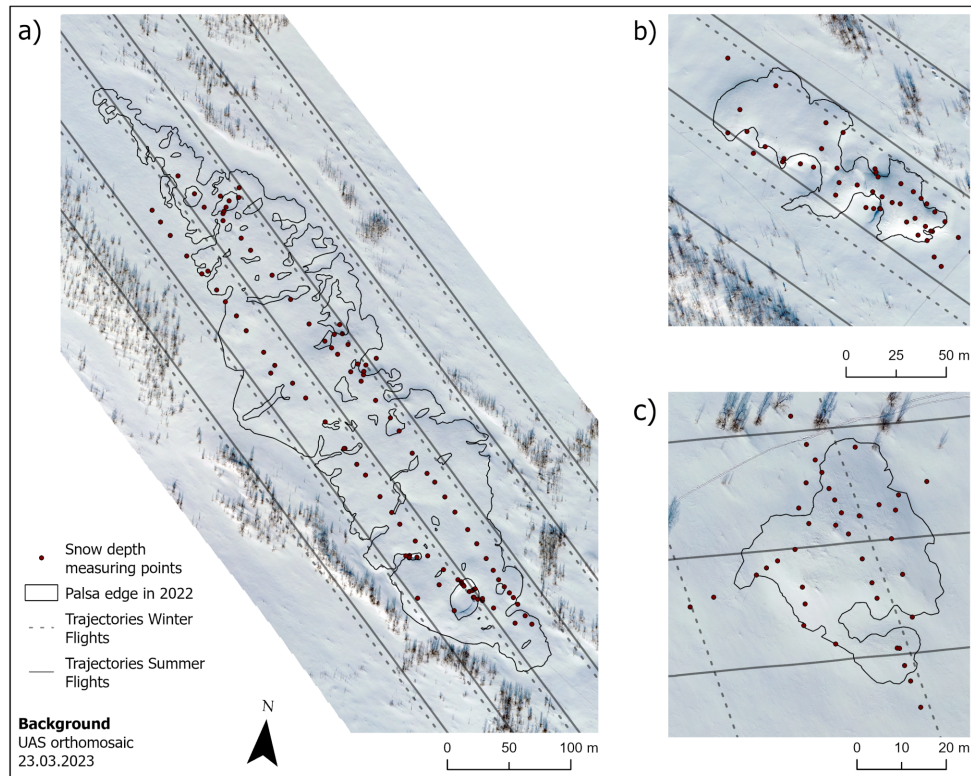
Figure 4. Snow depth measuring points within the investigation sites at Puolikkoniva (a), Pousu (b) and Peera (c) palsa illustrating different methods for recording snow depth (transects, randomized, crossed).

3.3   Modeling data preparation

220   The collected LiDAR data from the summer flight missions were used to create the input parameters for the RF modeling in *SAGA GIS* by SourceForge. For that, we used the created DTMs as input for the creation of all parameters and afterwards resampled these ~~raster~~ rasters to the same extent and resolution in *ArcGIS Pro*, making it suitable for analysis with the RF algorithm.

Subsequently, *SAGA GIS* was used for the computation of various geomorphological parameters to enhance the training dataset
225   with a diverse range of topographical and environmental predictors. These predictors included elevation, aspect, slope, and a range of indices comprising hydrological and morphological landscape features (Table 2). According to Meloche et al. (2022) and Revuelto et al. (2020), the *Topographic Position Index* (TPI) is of great relevance when modeling snow distributions due to its proven importance for representing dependencies between topography and snow depth.

Table 2. Overview of all input parameter used in the RF modeling.

Parameter	Description
Aspect	Aspect in degree of every raster cell (Olaya, 2009).
Channel Network Base Level	Provides information about channel networks and interpolates the base level elevations of it (Olaya and Conrad, 2009).
Channel Network Distance	Gives information about the vertical distance from altitudes above the channel network to its base (Olaya and Conrad, 2009).
Elevation	The elevation calculated from remote sensing data in Agisoft Metashape Professional.
Negative Openness	Parameter which indicates how enclosed the location of a landscape is (Yokoyama et al., 2002).
Positive Openness	Parameter which indicates how dominant the location of a landscape is (Yokoyama et al., 2002).
Relative Slope Position	Provides a measure of each cell's position in relation to the surrounding terrain (Böhner and Selige, 2006).
Slope	Slope in degree of every raster cell (Olaya and Conrad, 2009).
Topographic Position Index	Describes the relative elevation of a point compared to its surrounding terrain and is used to classify landforms. Positive values indicate ridges, negative values indicate valleys, and values near zero represent flat or uniform slopes (Guisan et al., 1999; Wilson and Gallant, 2000).
Valley Depth	Calculates the depth of valleys by finding the difference between each cell's elevation and an interpolated ridge level, where positive values indicate areas below the interpolated ridges, representing valleys, and negative values describing elevated regions like hills or ridges (Conrad et al., 2015).
Wind Effect	The index is a dimensionless measure used to assess terrain exposure relative to a specific wind direction. Values below 1 indicate areas sheltered from the wind, while values above 1 refer to regions exposed to wind (Gerlitz et al., 2015).
Wind Exposition	It assesses the overall terrain exposure to wind by considering all possible wind directions (Gerlitz et al., 2015). Unlike *Wind Effect*, this index calculates an average exposure value across multiple directions. Values below 1 indicate sheltered areas, while values above 1 signify wind-exposed regions.

3.4 Random Forest algorithm

230 For the modeling process, we used the **ranger** package (Wright and Zigler, 2017) within the R programming environment, which is known for its ability to efficiently process large datasets and accounts for complicated predictor interactions. The preparatory steps included aggregating the various input parameters into a uniform raster stack, conducted by the *stack* function from the **raster** package (Hijmans et al., 2023), ensuring spatial alignment across all layers.

The dependent variable for our model was the previous described $SD_{in\text{-}situ}$. These measurements, together with the stacked input parameters (Table 2) as independent variables, formed the basis of our RF model. The $SD_{in\text{-}situ}$ locations, serving as the training dataset, were buffered by 0.3 m, with each buffered point assigned to the corresponding snow depth value. The process of extracting input parameter values from the stacked raster set was performed by randomly separating 70% of the point features from each $SD_{in\text{-}situ}$ dataset for training and 30% for testing. After this separation we extracted the input parameter values for the training dataset, ensuring a clear distinction between training and testing data. The input parameters were not averaged within the buffer areas; instead, each parameter value was directly linked to the respective $SD_{in\text{-}situ}$ measurement. Consequently, each snow depth value is associated with an average of 28 input parameter values, leading to a dataset consisting of 3645 training values (Puolikkoniva 1983; Pousu 905; Peera 757) and 1577 test values (836; 401; 340). The buffering strategy aimed to moderate model variability, reduce noise, minimize the influence of geolocation and sampling errors, and enhance the robustness of the model by increasing the number of training points. By incorporating groupings of nearby points rather than relying on single-point measurements, this approach helps improve the model's stability and realism, as demonstrated in Bergamo et al. (2023). To prevent errors and miscalculations, all *NoData* values were removed from the datasets, resulting in a final training dataset of 3504 points and a final test dataset of 1548 points for further modeling and validation.

To determine the optimal values for *mtry*, *min.node.size*, and *sample fraction*, we performed hyperparameter tuning using the **mlr** package in R (Bischl et al., 2016). To prevent overfitting, we restricted the search range for *min.node.size* to 10–15 and for *sample fraction* to 0.7–0.85, following the recommendations of Probst et al. (2019) and Breiman (2001). Allowing an unlimited search range initially resulted in better model performance, but at the cost of reduced generalization, indicating signs of overfitting. We selected the final search range based on multiple test runs with different settings. For cross-validation, we tested different fold sizes to identify the most effective configuration. The best results were achieved using a 4-fold cross-validation. The final tuned hyperparameters values were as follows: *mtry*: 9; *min.node.size*: 10; *sample fraction*: 0.79.

Permutation mode was chosen for variable importance assessment, and a specific seed value was implemented to ensure reproducibility of the results. For more robustness, we repeated the calculation 100 times to obtain a mean permutation importance (PI) value for each input parameter, ensuring reliable rankings. The resulting PI values for each input parameter were normalized for better comparison by setting the most important parameter to 1. Subsequently, the trained RF model was employed to calculate SD_{RF} predictions across each palsa site by using the *predict* function.

Additionally, a correlation analysis between the input parameters and predicted SD_{RF} was performed to identify any correlating predictors and assess the strength of the relationships between them and the prediction. Correlation values for all input parameter are listed in Appendix A3. Furthermore, the RF model was run three additional times to ensure a fully external validation. In each run, one palsa site was excluded from the training data, allowing its measured $SD_{in\text{-}situ}$ values to be used exclusively for validation.

3.5 Statistical analysis

The statistical analysis focused on evaluating the predictive accuracy of the model. The following metrics were summarized for all palsa sites and calculated in the R environment:

1. **Coefficient of Determination (R^2):** Calculated to quantify the proportion of variance in the dependent variable that is predictable from the independent variables in the model (Nagelkerke, 1991), giving clearance about the overall effectiveness of the model, defined as

$$R^2 = 1 - \frac{\sum(y_i - \hat{y}_i)^2}{\sum(y_i - \bar{y})^2} \tag{1}$$

2. **Root Mean Square Error (RMSE):** Employed to quantify the average magnitude of the error in the predictions (Chai and Draxler, 2014), highlighting the ability of the model to predict snow depth accurately, defined as

$$\text{RMSE} = \sqrt{\frac{1}{n}\sum(y_i - \hat{y}_i)^2} \tag{2}$$

3. **Mean Absolute Error (MAE):** Measures the average magnitude of the absolute errors between predicted and observed values, without considering their direction (Chai and Draxler, 2014; Willmott and Matsuura, 2005), defined as

$$\text{MAE} = \frac{1}{n}\sum_{i=1}^{n}|y_i - \hat{y}_i| \tag{3}$$

4. **Standard Deviation (SD):** Provides a measure of the dispersion of prediction errors around their mean (Walser, 2011), revealing the precision and consistency of the predictions, defined as

$$\text{SD} = \sqrt{\frac{1}{n-1}\sum_{i=1}^{n}(y_i - \hat{y}_i)^2} \tag{4}$$

where y_i is the observed value, $\hat{y}_i$ is the predicted value from the model, $\bar{y}$ is the mean of observed values.

To visualize the statistical analysis results, scatter plots were created to compare RF and UAS LiDAR derived snow depths with the test dataset values.

4 Results

4.1 Snow depth predictions

In general, the predicted SD_{RF} present a good visual alignment with the calculated SD_{LiDAR} (Fig. 5).

The **Puolikkoniva** palsa site is affected by several collapsed areas, in which snow accumulates heavily. This can be seen in the SD_{RF} (Fig. 5 a) as well as in the SD_{LiDAR} (Fig. 5 b) results. At the eastern side of the palsa, RF models the snow depth inside these collapsed holes and cracks higher than the UAS LiDAR was detecting it. Especially directly at the steep edges of the palsa, the depth values increase up to 20 - 40 cm, partly up to 60 cm. At the western side of the palsa, SD_{LiDAR} is higher at these parts with values increasing up to 20 - 40 cm compared to SD_{RF}. However, the transition of the snow depths better corresponds to changes at slopes on the UAS LiDAR results, as the RF model reveals obvious patterns. The most obvious differences are occurring in areas beneath the palsa itself, for example the whole northeastern and eastern parts directly at the edge of the

palsa, which have higher snow depths (up to 60 cm) predicted by RF than detected based on the UAS LiDAR data. Within the open area beneath the palsa, SD_{LiDAR} is higher (up to 50 cm), following areas with higher vegetation. The most similar parts are the areas on top of the palsa with differences between both datasets under 15 cm, partly 20 cm. The UAS LiDAR dataset includes negative snow depth values, which result from elevation mismatches between the summer and winter DTMs. These are visualized in red to distinguish them clearly in Figure 5.

The **Pousu** palsa site shows a similar pattern as in the Puolikkoniva palsa site, with cracks filled by snow and collapsed parts with steep slopes where snow accumulated heavily (Fig. 5 c, d). Again, the transition of the snow depth at those areas is more natural in the SD_{LiDAR} data since the SD_{RF} data are showing sharp steps. Also, mire areas next to the palsa are observed by UAS LiDAR with lower snow depth as modeled with RF. This is especially visible in the southwestern and southern parts of the area, where snow depth was modeled between 40 – 50 cm and the UAS LiDAR detected values between 10 – 20 cm. However, similarities are visible on top of the palsa, where snow depths were modeled and observed in a range between 10 ~~to~~ and 30 cm each.

The **Peera** palsa site shows the highest consistency between SD_{RF} and SD_{LiDAR}. However, as in the two former sites, the highest snow depth accumulated in cracks and at the steep edges of the palsa (Fig. 5 e, f). Unlike at the other locations, there are no sharp steps at the parts mentioned here, as both approaches model smooth transitions. Similar structures are also visible on top of the palsa with snow depths around 20 cm in each approach. However, differences are visible like at the two other palsa sites in the surrounding area of the palsa, where the snow depth is calculated higher by RF than the UAS LiDAR detected it. Higher snow depths were also calculated with RF on the northwestern edge of the Palsa than measured with LiDAR (up to 30-50 cm). Viewing the deviations in snow depth between the two approaches, it is evident that the top parts of the palsa sites themselves show very low differences (Fig. 6 a, b, c). However, deviations occurred at the edges, inside of cracks, at the highest parts of the palsa and in the surrounding areas. Within cracks on top of the palsa sites, the UAS LiDAR detected in general higher snow depth than RF modeled it, except for the eastern side of Puolikkoniva palsa, where it is the other way around. Differences of around 20 cm are shown, but with peaks up to 60 cm. Also, highest elevated structures of the palsa sites directly at edges show deviations of about 15 - 40 cm higher snow depth calculated by the UAS LiDAR, except for Peera palsa. In contrast, the collapsed parts with accumulated snow are consistently modeled with higher values exceeding 45 cm of deviation to the UAS LiDAR derived values. Notably, deviations in the areas surrounding the palsas are primarily characterized by higher snow depths predicted by the RF model, with exception for areas with higher vegetation at Puolikkoniva palsa site.
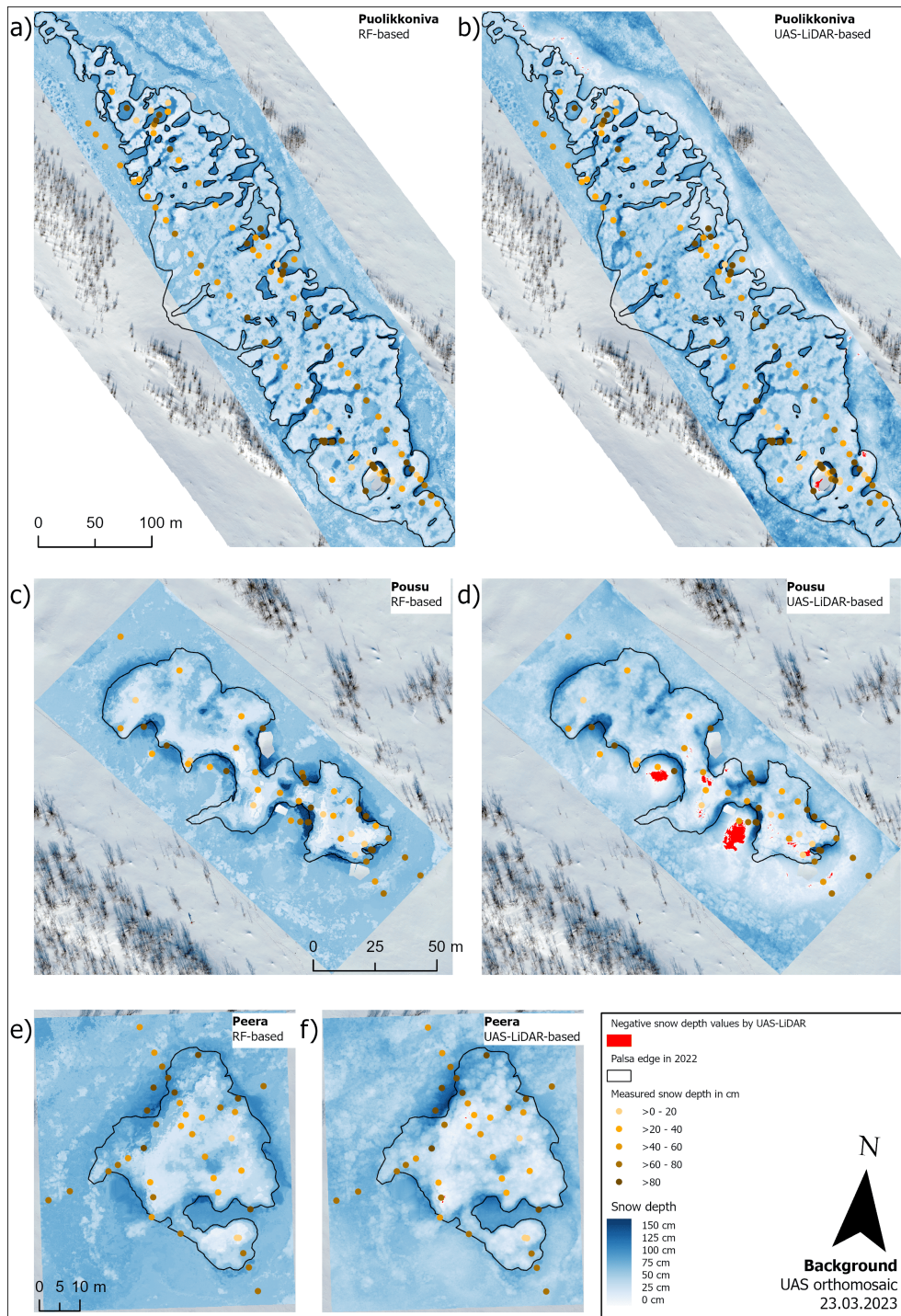
Figure 5. Snow depth predictions based on the RF model (left) and the UAS LiDAR (right) at site Puolikkoniva (a, b), Pousu (c, d) and Peera (e, f) palsas. Red points ~~are showing~~ indicate SD$_{in\text{-}situ}$ locations and represent measured snow depth. In the LiDAR results, red-colored areas correspond to negative snow depth values, which result from elevation mismatches between the summer and winter DTMs.
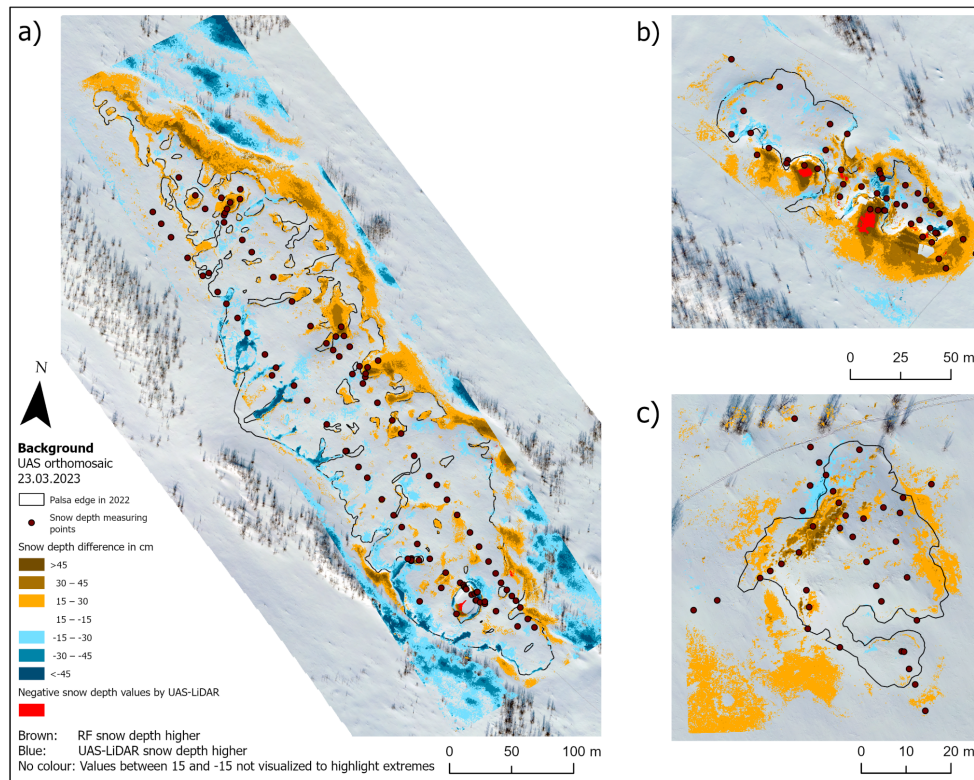
Figure 6. Snow depth differences between modeled and UAS LiDAR results at a) Puolikkoniva, b) Pousu and c) Peera palsas.

4.2 Variable importance

The calculated PI values of all parameters are pictured in Fig. 7. The four most important parameters are *TPI, Wind Exposition, Elevation, and Channel Network Base Level*, while *TPI* is the most important parameter and set to 1. It is more than four times more ~~important~~ significant than the two following parameters *Wind Exposition* (around 0.14) and *Elevation* (0.13). In addition, *Channel Network Base Level* (0.12), *Wind Effect* (0.08) and *valley Depth* (0.07) are also of substantial importance. The remaining input parameter *Positive Openness, Channel Network Distance, Relative Slope Position, Negative Openness, Slope, Aspect* possess lower importance than 0.04.
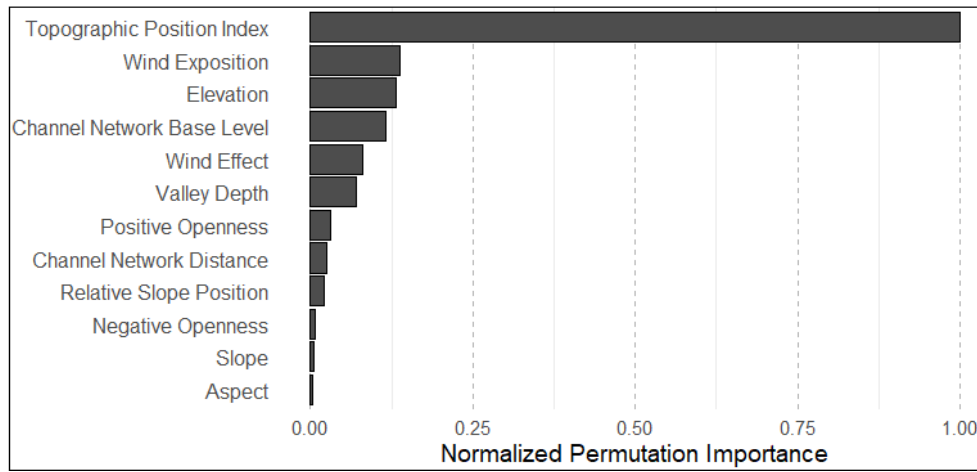
Figure 7. Overview of normalized mean Permutation Importance values from RF modeling over 100 iterations.

4.3   Statistical evaluation results

The statistical analysis of the general (Table 3) and validation point locations accuracy (Table 4) reveals comparable high
accuracy of SD_{RF} and SD_{LiDAR}. The RF modeling dataset has slightly better statistical validation metrics than the SD_{LiDAR}
dataset with a RMSE of 18.33 cm compared to 23.49 cm. Furthermore, R^2, MAE and SD are better in the RF modeling with
values of 0.770, 13.26 cm and 18.11 cm compared to 0.691, 17.49 cm and 20.84 cm. The external validation results of the RF
modeling dataset for each palsa (Table 3) indicate the best performance at the Peera site, with an RMSE of 16.67 cm and an
R^2 of 0.628. At the Pousu site, the RMSE is higher (21.31 cm), but the R^2 improves to 0.767. The Puolikkoniva site shows the
weakest performance, with both metrics being the lowest: an RMSE of 27.13 cm and an R^2 of 0.578.

When analysed by point groups, the SD_{RF} and SD_{LiDAR} results show strong similarities for the *On Top* and *Edge* classes, while
the *Thermokarst* and *Open Area* classes exhibit better metrics in the SD_{RF} dataset. RMSE and MAE values are identical for
both datasets in the *On Top* (8.33 cm, 3.84 cm) and *Edge* (13.12 cm, 5.85 cm) groups, but R^2 is higher for SD_{RF} (*On Top*: 0.841,
Edge: 0.894) compared to SD_{LiDAR} (0.730, 0.768). A similar trend is observed for standard deviation, with values of 8.32 cm
versus 10.83 cm in the *On Top* class and 12.82 cm versus 19.09 cm in the *Edge* class. The *Thermokarst* class consistently shows
better metrics in SD_{RF} compared to SD_{LiDAR}, with RMSE of 10.99 cm compared to 33.73 cm, R^2 of 0.893 to 0.592, MAE of
5.42 cm to 30.35 cm and SD of 10.69 cm to 25.08 cm. A similar pattern is observed for the *Open Area* class, where RMSE
improves from 14.23 cm (SD_{LiDAR}) to 4.45 cm (SD_{RF}), R^2 from 0.519 to 0.926, MAE from 9.84 cm to 1.56 cm, and SD from
12.59 cm to 4.40 cm.

Table 3. Overview of the calculated Root Mean Square Error (RMSE) in cm, Coefficient of Determination (R^2), Mean Absolute Error (MAE) in cm and Standard Deviation (SD) in cm for RF- and UAS LiDAR-derived snow depth estimations. Additionally, external validation results ~~(RMSE and R^2)~~ for RF-modeled snow depth at each palsa site (Peera RF, Pousu RF, Puolikkoniva RF) are provided.

Parameter	RF	LiDAR UAS	Peera RF	Pousu RF	Puolikkoniva RF
RMSE	18.33	23.49	16.67	21.31	27.13
R^2	0.770	0.691	0.628	0.767	0.578
MAE	13.26	17.49	−12.56	−15.78	-21.44
SD	18.11	20.84	−15.70	−19.63	-26.82

Table 4. Overview of RMSE in cm, R^2, MAE (cm) and SD (cm) divided by validation point locations within the investigation areas.

	RMSE		R^2		MAE		SD	
	RF	*LiDAR*	*RF*	*LiDAR*	*RF*	*LiDAR*	*RF*	*LiDAR*
On Top (n = 69)	8.33	8.33	0.841	0.730	3.84	3.84	8.32	10.83
Edge (n = 66)	13.12	13.12	0.894	0.768	5.85	5.85	12.82	19.09
Thermokarst (n = 16)	10.99	33.73	0.893	0.592	5.42	30.35	10.69	25.08
Open Area (n = 26)	4.54	14.23	0.926	0.519	1.56	9.84	4.40	12.59

345 The presented scatter plots of both approaches (Fig. 8) are revealing further insights into the accuracy of the results. Both SD_{LiDAR} (left plot) and SD_{RF} (right plot) show a positive correlation with the $SD_{in-situ}$. The regression line in both plots closely follows the expected trend, showing that both methods capture snow depth patterns well. The $SD_{LiDAR RF}$ ~~have~~ results exhibit a tighter spread around the regression line, indicating lower variance compared to ~~the~~ $SD_{RF LiDAR}$. This is consistent with the standard deviation values reported in Table 4, where SD_{RF} shows a 13–65% lower spread across validation point groups. The

350 spread of residuals (black dots deviating from the regression line) increases with snow depth in both cases, ~~indicating~~ indicate larger uncertainty for deeper snow, while the confidence intervals remain narrow at lower snow depths. A single negative outlier is present for SD_{LiDAR}.

In addition, the correlation analysis between the input parameters and SD_{RF} reveals a strong negative correlation with *TPI* (-0.87) and *Wind Exposition* (-0.80). Moderately high negative correlations are observed for *Wind Effect* (-0.50), *Positive*

355 *Openness* (-0.50), *Relative Slope Position* (-0.49), and *Channel Network Distance* (-0.45). The only moderately high positive correlation is given for *Valley Depth* with 0.50. All other parameters show low correlation, with values close to zero.
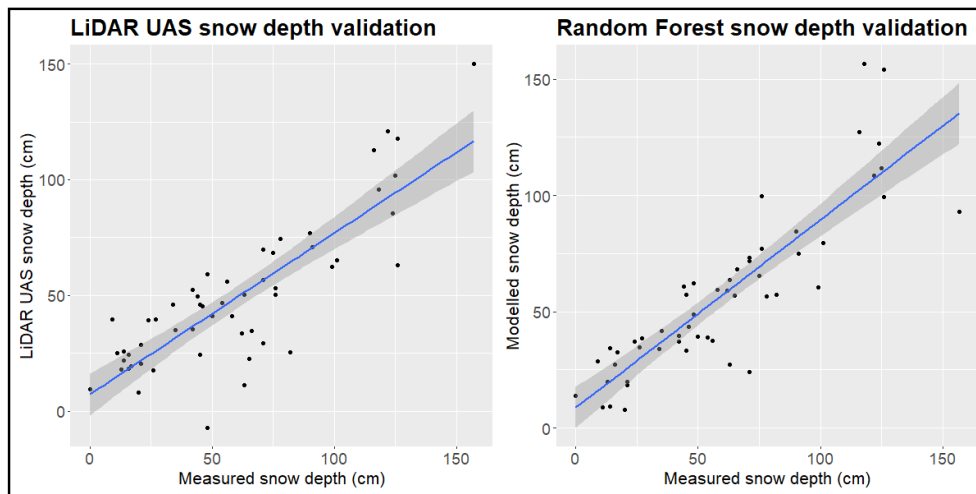
Figure 8. Scatter plots with regression lines for UAS LiDAR-derived and RF-modeled snow depths, based on the external test dataset.

5 Discussion

5.1 Analysis of RF and LiDAR snow mapping

The statistical analysis of SD_{RF} and SD_{LiDAR} demonstrates statistically significant and reliable results for both approaches. The overall metrics of RMSE and R^2 for RF and LiDAR, indicating a slightly better performance of the RF model in mapping snow distribution (Table 3). This trend is also evident in the visual comparison, though a more detailed examination reveals important differences between the two methods. The external validation across all palsa sites confirms the sufficient accuracy of the RF model (Table 3), while the scatter plots (Fig. 8) show a strong consistency between the two approaches.

In both approaches, the upper parts of the palsa, which are relatively flat and covered with low vegetation, have similar snow depth values. This is also confirmed by the identical RMSE for the point group *On Top* (Table 4). Since these areas are well represented in the training dataset for the RF approach and the surface captured by UAS LiDAR changes only slightly between summer and winter in the stable area of the palsa, both methods perform well in estimating snow depth. The accuracy of the RF models depends to a large extent on the quality of the training data, which is the reason ~~why~~ a well-distributed dataset is essential. However, as the surface variations on the top of the palsas are minimal, the acquisition of representative training data is relatively easy, which explains the high accuracy of the model in these areas. The same considerations apply to the UAS LiDAR data. Due to the low vegetation cover, only minimal vegetation removal was required during post-processing, reducing potential sources of error in these areas. However, the seasonal changes in ground level in palsa mires must also be taken into account. Frost heave and subsidence cause natural height variations of several centimeters between summer and winter, as recently described by Renette et al. (2024). If the UAS LiDAR dataset is acquired in spring immediately after snowmelt, when the ALT has reached its minimum thawing depth, such effects could be minimized. In addition, RTK GPS point data from field measurements in winter and summer could help to correct elevation differences by calculating mean elevation shifts. However,

this method has its own challenges, as measuring ground level in winter is difficult due to the overlying snow cover. These seasonal variations in elevation should be carefully considered when deriving snow distribution from multi season DTMs. In contrast, RF is expected to be less affected by this problem as the modeled snow depth values are derived from training data

380 and are not directly based on the absolute elevation differences between summer and winter datasets.

Similar patterns are observed for the steep edges of the palsa. While the RF model performs lowest for the *Edge* point class within its own results, the LiDAR approach achieves its second best performance in this category. Despite these internal differences, both methods produce identical RMSE values of 13.12 cm (Table 4). However, when interpreting LiDAR data, there are additional challenges at the palsa edges due to continuous degradation processes that lead to differences between the

385 summer and winter DTMs. During summer data collection, palsa edges are recorded before block erosion occurs, meaning that loose soil remains intact. By winter, block erosion and soil displacement may alter the terrain, leading to higher deviations between the DTMs. As a result, the SD$_{LiDAR}$ values are artificially increased even though the actual snow depth is lower. A similar problem arises if cracks form after data collection in summer, which accumulate snow in winter and further increase the calculated snow depths. At the same time, these degradation processes are also not considered in the RF approach, as the

390 summer dataset was used to derive all input parameters. This explains why RF struggles the most at the edges. In addition, the redistribution and accumulation of snow on steep slopes is a highly dynamic and chaotic process that is difficult to capture with high precision.

In contrast to other areas of the palsa, the RF and UAS LiDAR approaches show the lowest agreement over ~~open water thermokarst pond~~ areas, which is reflected in the statistical metrics for the *Thermokarst* point class. ~~While the RF model~~

395 ~~estimates snow depth in these areas more accurately than at the palsa edges, UAS LiDAR performs lowest in this category. This can be attributed to~~ Although these areas are snow-covered during winter LiDAR acquisition, they are characterized by open water surfaces in the summer dataset used to derive snow depth by DTM subtraction. This leads to an underestimation of terrain height in the summer DTM due to the low reflectivity and absorption of the LiDAR signal over water surfaces (Mandlburger and Jutzi, 2019), resulting in an overestimation of snow depth. In contrast, RF modeling benefits from the ~~well~~

400 ~~documented problems with low reflective surfaces such as water (Mandlburger and Jutzi, 2019) and the difficulties in detecting highly scattering materials such as snow (Deems et al., 2013). However, RF takes advantage of the~~ contextual relationships between the ~~input~~ terrain parameters and the observed snow depth ~~on~~ over thermokarst ponds and can ~~therefore compensate for incorrect initial values in the UAS LiDAR dataset and keep a high performance~~ partially compensate for such systematic errors, maintaining higher accuracy. Even though volumetric scattering in snow can affect LiDAR results, the associated error

405 at wavelengths commonly used for snow depth measurements, such as the 905 nm wavelength applied in this study, is typically in the low centimeter range (Deems et al., 2013), and thus does not account for the larger discrepancies observed in this study. In addition, in mire areas surrounding the palsa, such as the statistics for *Open Area* point class shows it, the RF model performs with the highest accuracy within its own results, while UAS LiDAR ranks second lowest. However, for UAS LiDAR, the deviation from the two best-performing groups *On Top* and *Edge* remains relatively small, indicating a consistent performance

410 across the dataset. A significant challenge in these areas is the seasonal vegetation dynamics. In summer, the vegetation in palsa mires grows taller and denser, while in winter the grasses and sedges are compressed under the weight of the snow. The

LiDAR sensor records all surface elements, i.e. the vegetation in summer and the snow covered areas in winter. Despite the removal of vegetation in post-processing, a residual bias remains due to the dense vegetation, which cannot be completely filtered out from the ground, leading to a systematic underestimation of snow depth in areas with height changing vegetation.

415 Similar problems with LiDAR-derived snow depth mapping were reported by Broxton et al. (2019). Tall shrubs such as *Betula nana*, which form thickets at palsa edges, can further complicate capturing the palsa surface in detail. In contrast, the RF model inherently accounts for vegetation as it uses UAS LiDAR summer data as the basis for calculating input parameters. By integrating $SD_{in\text{-}situ}$ measurements from winter, RF can establish relationships between vegetation and snow accumulation, which reduces bias and improves snow depth estimation. Methods to further improve LiDAR-derived snow depth mapping,

420 such as correcting estimates based on vegetation type, density and height, could help to mitigate these limitations.

These results confirm that snow distribution can be accurately modeled at a small-scale using low cost equipment, such as a yardstick, in combination with moderate computational resources. However, we acknowledge that an expensive LiDAR sensor was used in this study to derive the input parameters for the RF model. Therefore, further research should investigate if low cost UAS RGB data can provide equally high quality input parameters or if LiDAR is still essential for accurate modeling.

425 Recent studies by Harder et al. (2020) and Cho et al. (2024) have shown that snow depths derived from UAS LiDAR data provide a more accurate representation of snow distribution than snow depth products derived from UAS RGB data, which raises the question ~~of~~ whether the use of RGB-derived input parameters is feasible for modeling purposes. However, for large-scale spatial snow distribution overviews or in cases where high-resolution snow depth mapping is not required, UAS LiDAR or RGB data might be preferable, as manual snow depth measurements are connected with a high workload and considerable

430 time investment. Furthermore, the potential of UAS imagery for snow depth estimation has been investigated in several recent studies (Marti et al., 2016; Rauhala et al., 2023; Revuelto et al., 2021; Walker et al., 2021), emphasizing its growing importance for snow distribution monitoring.

5.2 Snow distribution mapping in palsa mires and its impacts

The high-resolution snow depth maps produced in this study provide a detailed spatial representation of snow distribution

435 patterns in palsa mires and highlight pronounced warming and cooling areas. Both the LiDAR and RF datasets show similar small-scale variations that are closely linked to topographic features. These findings suggest that the observed snow distribution patterns accurately reflect the actual conditions in the studied palsa landscapes, making them valuable for assessing the potential interactions between snow accumulation and palsa thermal dynamics.

Warming areas in the palsas were identified at the edges of the palsa and in cracks where snow accumulates due to wind

440 transport and gravitational sliding. This effect is consistent with the findings of Peng et al. (2024), who showed that snow accumulations insulate the ground and reduce the penetration of cold air. An example of this effect can be seen at Pousu Palsa (Fig. 9 d, e), where the dominant south and southwest winds (FMI data for the last 20 years from the Kilpisjärvi weather station) contribute to the highest snow accumulation on the southwestern and northeastern edges. Snow accumulation in these areas extends snowmelt into late spring and summer and increases soil moisture, which can increase heat transfer to the soil. While

445 an extended snow cover reduces direct solar radiation, it also prevents deep freezing in winter, which can destabilize ice core

edges. This also leads to a thinner ALT at the edges, as the solar radiation remains limited due to the longer-lasting snow cover. These observations are consistent with the results of Verdonen et al. (2023) and Seppälä (2011). Such processes can contribute to block erosion and expose the frozen core to further thawing. The formation of cracks in the upper edge zones could also increase this effect, as they fill with snow in winter, delaying freezing and possibly further accelerating the instability of the

450 palsa. These results are consistent with those of Martin et al. (2021), who showed that palsas undergo structural adjustments at constant snow depths of 20-30 cm. However, our results indicate that in the Kilpisjärvi region, even greater snow depths occur at the palsa edges, suggesting that the increasing snow accumulation may be linked to the continuing degradation of the palsas. This cycle continues until the palsa slopes flatten, reducing snow accumulation, which eventually leads to the degradation of the upper plateau. Long-term ALT and permafrost temperature measurements at these sites are needed to confirm this hypothesis.

455 As ~~suggested~~ proposed by Seppälä (2011), snow conditions may play a more important role in the development of Palsa than previously thought. Continued monitoring and integration of these findings into permafrost models will be essential for a better understanding of future palsa development.

~~Uppermost~~ The uppermost parts of the palsa summits are cooling areas, where thin layers of snow allow cold air to penetrate deeper, which promotes ice core stability in winter. Seppälä (2003) proved that a thicker snow cover on the palsas delays the

460 melting of the ice core due to its prolonged presence. Conversely, this means that cooling areas have deeper ALT in summer than warming areas. As observed at Pousu Palsa (Fig. 9 b, c), the cooling areas are concentrated ~~near~~ at the uppermost parts of the steep edges, where the surface is highly exposed to the wind. Further investigation is needed to determine whether this, combined with destabilization and edge collapse, contributes to the formation of steep or even vertical slopes. If this process continues, cracks may eventually form, causing block erosion and degradation of the palsa edge.

465 The findings of this study suggest that snow depth variability plays a crucial role in the stability of the palsa, with small-scale redistribution patterns influencing local permafrost dynamics. However, as this analysis is only based on snow depth data, further research combining continuous monitoring of snow depth with thermal observations of permafrost is needed to confirm these interactions. Establishing a direct link between snow accumulation patterns and thermal processes in the subsurface would provide valuable insights into the long-term evolution of palsa mires under changing climatic conditions. Furthermore,

470 our study indicates that there is a clear need for more detailed research on the interaction between tall shrubs, snow depth, and permafrost.

a) Pousu palsa site and the analysis area (red).

b) Slope in degrees.

c) Differences in snow depth between RF and LiDAR UAS approach.

d) Snow distribution based on RF approach and highlighted cooling and warming locations.

e) Possible warming/cooling spots based on snow distribution and areas with existing or higher possibility of block erosion.
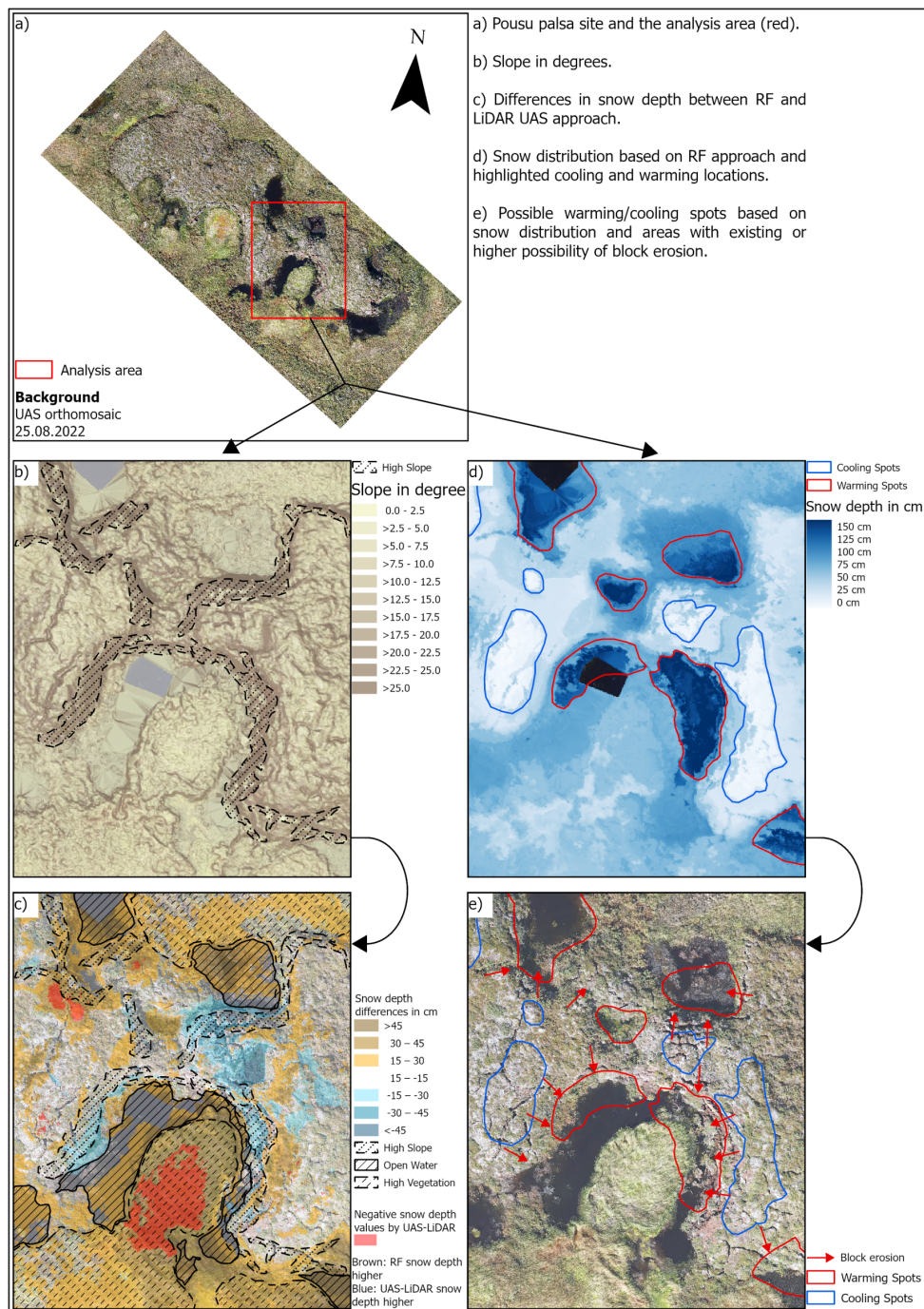
Figure 9. ~~Explanation~~ Demonstration of differences between UAS LiDAR-derived and RF-modeled snow depths.

5.3 Uncertainties and limitations

Snow distribution is highly variable, especially because of wind drifts and topography, which must be considered when applying these methods. Additionally, machine learning models rely on a unique observation in time. Changing weather conditions could result in a completely different snow distribution on another day, which could affect model performance.

~~Various~~ Several sources of error ~~may be present during data collection in~~ can affect LiDAR-derived snow depth measurements during both summer and winter data acquisition. Reflective or complex surfaces, such as water or vegetation, may scatter or block the laser signal, introducing measurement biases and limiting surface detectability (Deems et al., 2013; Gould et al., 2013). ~~LiDAR sensors in particular are prone to inaccuracies; highly reflective surfacescan cause scattering of the laser beam, leading to a bias in the data (Deems et al., 2013). In addition, shrub vegetationcan hide the surfaces and prevent them from being fully captured (Gould et al., 2013).~~ These distortions ~~affect~~ impact the entire modeling approach as they influence the calculation of the input parameters. ~~The~~ Another source of uncertainty is the choice of LiDAR wavelength~~is another critical factor, as the use of different or multiple wavelengths has been shown to improve the accuracy of snow depth mapping (Deems et al., 2013).~~ The 905 nm wavelength used in this study is typical for many airborne systems and generally produces only minor depth errors in snow due to limited penetration, with most of the signal returned from the upper centimeters of the snowpack (Deems et al., 2013). In comparison, shortwave infrared wavelengths such as 1550 nm are more strongly absorbed by ice, resulting in a return signal that is more confined to the snow surface. This characteristic can help reduce uncertainty, particularly in areas with complex surface conditions or low reflectivity. While the wavelength-related interaction with the snow surface is a key factor, detailed information on snow conditions, such as grain size, snow age, or impurity content, was not collected during the field campaign. Such data could, however, help to better assess potential sources of uncertainty in the LiDAR-derived snow depth, particularly those related to scattering and absorption effects. Errors can also occur when collecting training data, albeit to a less significant extent. Measuring with a yardstick is a reliable method of measuring snow depth, but dense layers of ice or vegetation close to the ground, such as roots, can change the recorded values by a few centimeters, as the ground surface was incorrectly assumed. In areas with denser vegetation, the probe may not always reach the exact ground surface, resulting in a slight underestimation of the snow depth. This could affect both the training and validation of the RF model and the accuracy of the LiDAR-derived snow distributions, thus affecting the statistical performance of the results. Devices that have been developed only for taking snow depth values, such as a GPS Magnaprobe, as used in a study by Walker et al. (2021), could minimize such possible errors.

The selection of input parameters is another aspect that requires critical evaluation. The TPI plays a central role in the model, as it combines several topographic features into a single parameter. As snow tends to accumulate at the edges and drift down the slopes, its movement from one grid cell to the next is effectively captured by the TPI, making it a crucial variable for the model. This finding is in line with studies by Revuelto et al. (2020) and Meloche et al. (2022), which highlight the importance of the TPI for modeling snow distribution. Other important parameters are related to wind properties and basic surface structures, which emphasizes the importance of wind drift and steep edges in snow distribution formation. However, it should be noted that the selected parameters represent only a fraction of the potential variables that influence snow distribution. The RF model

is theoretically capable of incorporating a larger set of parameters and still identifying the most ~~important~~ significant ones. For example, detailed vegetation classifications - including specific vegetation types or density indices - could further improve snow depth modeling. In addition, there are influencing factors that, while not directly related to snow depth, can still have an impact on snow distribution patterns. The identification of such variables would require a specific study aimed at evaluating and selecting the most important parameters for snow depth modeling.

6 Conclusions

We present an analysis of snow distribution in palsa mires using a combination of *in-situ* measurements, UAS LiDAR data, and RF modeling. This study provides valuable insights into small-scale snow distribution, revealing distinct accumulation patterns at palsa edges and cracks, driven by wind effects and gravitational sliding. The increased snow depth in these areas prolongs snowmelt, which could influence thermal insulation and ALT dynamics of permafrost. In contrast, the exposed palsa areas exhibit thinner snow cover, promoting deeper frost penetration in winter but also greater exposure to solar radiation in summer. Statistically, both RF modeling and UAS LiDAR provided reliable results for mapping snow distribution with an RMSE of 18.33 cm (RF) and 23.49 cm (LiDAR) and corresponding R^2 values of 0.77 and 0.691. While the RF model showed slightly better prediction performance, the differences between the two approaches remained moderate. This indicates that RF modeling is a promising ~~alternative~~ approach for snow depth estimation, especially when appropriate input parameters such as TPI and wind-related parameters are included. At the same time, UAS LiDAR provides a direct, high-resolution snow depth dataset and is therefore a valuable tool for spatial snow mapping.

Our results highlight the vulnerability of Palsas to changes in snow depth patterns due to climate warming. A change in snow depth and altered wind dynamics could further accelerate the degradation of Palsas and lead to a progressive loss of permafrost soils in northern Finnish Lapland. Future studies should focus on integrating long-term permafrost monitoring with these snow distribution models to better understand the interactions between snow cover, permafrost thaw and climate change. The presented methodology provides a foundation for further modeling approaches that integrate snow distribution dynamics with permafrost development. While tested for palsa environments, the approach can also be applied to other pan-Arctic palsa areas, continuous permafrost regions, and even adapted for small-scale avalanche forecasting or surface process studies such as soil erosion or landform changes. In conclusion, this study demonstrates the feasibility of using both RF modeling and UAS LiDAR for high-resolution snow depth mapping in palsa mires.

Appendix A

A1
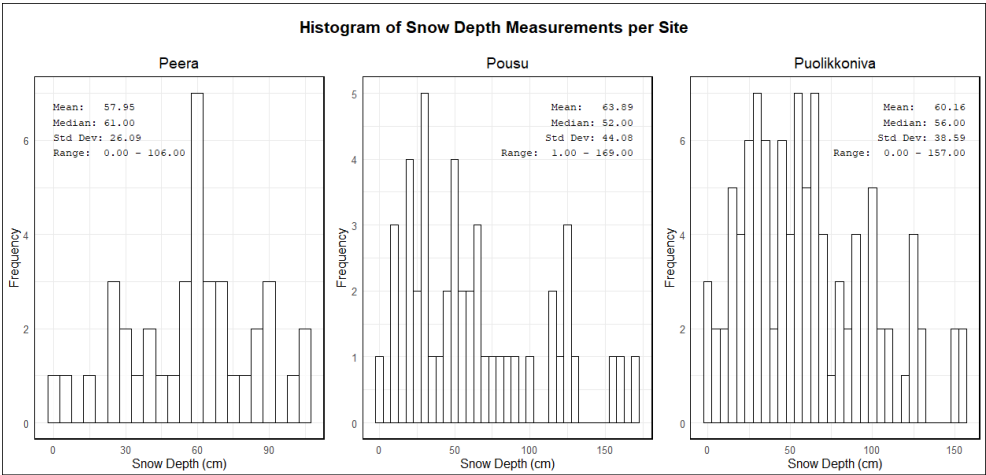
Figure A1. Histogram of SD$_{in\text{-}situ}$ points and respective statistics per palsa site.
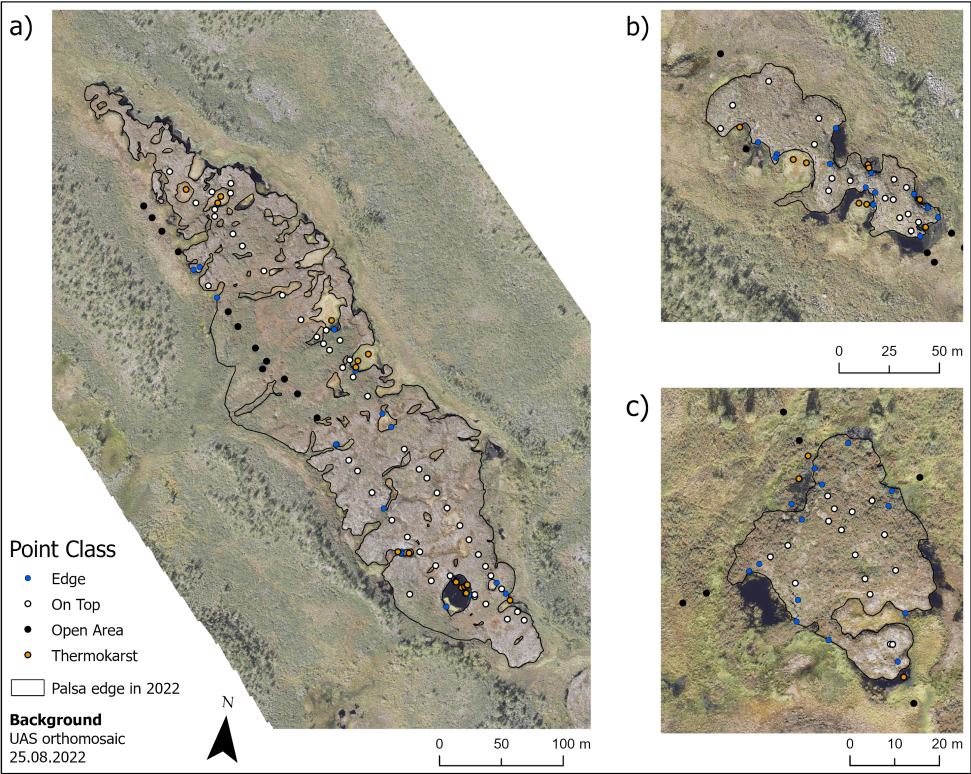
Figure A2. Overview of classification of all SD$_{\text{in-situ}}$ points into classes Edge, On Top, Open Area and Thermokarst.

535 **A3**

Table A1. Correlation between each input parameter and RF-modeled snow depth.

Parameter	Correlation to SD$_{\text{RF}}$	Parameter	Correlation to SD$_{\text{RF}}$
Aspect	0.09	Relative Slope Position	-0.49
Elevation	-0.12	Slope	0.08
Channel Network Base Level	-0.09	Topographic Position Index	-0.87
Channel Network Distance	-0.45	Valley Depth	0.50
Negative Openness	0.22	Wind Effect	-0.55
Positive Openness	-0.50	Wind Exposition	-0.80

Code availability. The R script used in this study is available upon request from the authors.

Data availability. Snow Depth and UAS data used in this study are available upon request from the authors. Meteorological data are available through the Finnish Meteorological Institute (https://en.ilmatieteenlaitos.fi/download-observations, FMI, 2024).

540

Author contributions. Initial study design: AS. Supervision: BB and TK. Data collection: AS, HS, MV, TK and PK. Data processing: AS, MV and PK. Data analysis and visualization of the results: AS, HS. Discussion of results and conclusions: AS, MV, BB and TK. Writing the paper: AS, with contribution from BB, TK, MV and HS.

Competing interests. The authors declare that they have no conflict of interest.

Financial support. AS, BB and HS has been supported by the European Union's ERASMUS+ staff mobility programme and by the Graduate Academy of the Leibniz University Hannover. TK, MV and PK were supported by LANDMOD project (the Academy of Finland grant no.

545 330319) and CHARTER project (EU Horizon 2020 Research and Innovation Programme grant no. 869471).

References

Autio, J. and Heikkinen, O.: The climate of northern Finland, Fennia, 180, 61–66, 2002.

Barry, R. G.: The Role of Snow and Ice in the Global Climate System: A Review, Polar Geography, 26, 235–246, https://doi.org/10.1080/789610195, 2002.

550 Bergamo, T. F., de Lima, R. S., Kull, T., Ward, R. D., Sepp, K., and Villoslada, M.: From UAV to PlanetScope: Upscaling fractional cover of an invasive species Rosa rugosa, Journal of Environmental Management, 336, https://doi.org/10.1016/j.jenvman.2023.117693, 2023.

Bischl, B., Lang, M., Kotthoff, L., Schiffner, J., Richter, J., Studerus, E., Casalicchio, G., and Jones, Z. M.: mlr: Machine Learning in R, https://github.com/mlr-org/mlr, 2016.

Breiman, L.: Random Forests, Machine Learning, 45, 5–32, 2001.

555 Broxton, P. D., van Leeuwen, W. J., and Biederman, J. A.: Improving Snow Water Equivalent Maps With Machine Learning of Snow Survey and Lidar Measurements, Water Resources Research, 55, 3739–3757, https://doi.org/10.1029/2018WR024146, 2019.

Böhner, J. and Selige, T.: Spatial Prediction of soil attributes using terrain analysis and climate regionalisation, Göttinger Geographische Abhandlungen, 115, 13–28, 2006.

Bühler, Y., Adams, M. S., Bosch, R., and Stoffel, A.: Mapping snow depth in alpine terrain with unmanned aerial systems (UASs): Potential 560 and limitations, The Cryosphere, 10, 1075–1088, https://doi.org/10.5194/tc-10-1075-2016, 2016.

Chai, T. and Draxler, R. R.: Root mean square error (RMSE) or mean absolute error (MAE)? -Arguments against avoiding RMSE in the literature, Geoscientific Model Development, 7, 1247–1250, https://doi.org/10.5194/gmd-7-1247-2014, 2014.

Chen, L., Aalto, J., and Luoto, M.: Observed Decrease in Soil and Atmosphere Temperature Coupling in Recent Decades Over Northern Eurasia, Geophysical Research Letters, 48, https://doi.org/10.1029/2021GL092500, 2021.

565 Cho, E., Verfaillie, M., Jacobs, J. M., Hunsaker, A. G., Sullivan, F. B., Palace, M., and Wagner, C.: Characterizing Spatial Structures of Field-Scale Snowpack using Unpiloted Aerial System (UAS) Lidar and SfM Photogrammetry, https://doi.org/10.5194/egusphere-2024-1530, 2024.

Conrad, O., Bechtel, B., Bock, M., Dietrich, H., Fischer, E., Gerlitz, L., Wehberg, J., Wichmann, V., and Böhner, J.: System for Automated Geoscientific Analyses (SAGA) v. 2.1.4, Geoscientific Model Development, 8, 1991–2007, https://doi.org/10.5194/gmd-8-1991-2015, 570 2015.

Deems, J. S., Painter, T. H., and Finnegan, D. C.: Lidar measurement of snow depth: A review, https://doi.org/10.3189/2013JoG12J154, 2013.

DeWalle, D. R. and Rango, A.: Principles of snow hydrology, Cambridge University Press, ISBN 9780511535673, https://doi.org/10.1017/CBO9780511535673, 2008.

575 EuroGeographics: EuroGlobalMap [data set], https://www.mapsforeurope.org/access-data, 2024.

FMI: Download observations, FMI [data set], https://en.ilmatieteenlaitos.fi/download-observations, last access: 09.08.2022, 2022.

FMI: Seasons in Finland, https://en.ilmatieteenlaitos.fi/seasons-in-finland, 2024.

Gerlitz, L., Conrad, O., and Böhner, J.: Large-scale atmospheric forcing and topographic modification of precipitation rates over High Asia - A neural-network-based approach, Earth System Dynamics, 6, 61–81, https://doi.org/10.5194/esd-6-61-2015, 2015.

580 Gould, S. B., Glenn, N. F., Sankey, T. T., and Mcnamara, J. P.: Influence of a Dense, Low-height Shrub Species on the Accuracy of a Lidar-derived DEM, Photogrammetric Engineering Remote Sensing, 79, 421–431, 2013.

Guisan, A., Weiss, S. B., and Weiss, A. D.: GLM versus CCA spatial modeling of plant species distribution, Plant Ecology, 143, 107–122, 1999.

Harder, P., Pomeroy, J. W., Helgason, W. D., and Helgason, W. D.: Improving sub-canopy snow depth mapping with unmanned aerial vehicles: Lidar versus structure-from-motion techniques, Cryosphere, 14, 1919–1935, https://doi.org/10.5194/tc-14-1919-2020, 2020.

Hijmans, R. J., van Etten, J., Sumner, M., Cheng, J., Baston, D., Bevan, A., Bivand, R., Busetto, L., Canty, M., Fasoli, B., Forrest, D., Ghosh, A., Golicher, D., Gray, J., Greenberg, J. A., Hiemstra, P., Hingee, K., and Ilich, A.: Package 'raster': Geographic Data Analysis and Modeling, https://doi.org/10.32614/CRAN.package.raster, 2023.

Hu, J. M., Shean, D., and Bhushan, S.: Six Consecutive Seasons of High-Resolution Mountain Snow Depth Maps From Satellite Stereo Imagery, Geophysical Research Letters, 50, https://doi.org/10.1029/2023GL104871, 2023.

IPCC: IPCC, 2023: Climate Change 2023: Synthesis Report. Contribution of Working Groups I, II and III to the Sixth Assessment Report of the Intergovernmental Panel on Climate Change [Core Writing Team, H. Lee and J. Romero (eds.)], https://doi.org/10.59327/IPCC/AR6-9789291691647, 2023.

Jacobs, J. M., Hunsaker, A. G., Sullivan, F. B., Palace, M., Burakowski, E. A., Herrick, C., and Cho, E.: Snow depth mapping with unpiloted aerial system lidar observations: A case study in Durham, New Hampshire, United States, Cryosphere, 15, 1485–1500, https://doi.org/10.5194/tc-15-1485-2021, 2021.

Kauhanen, H. O.: Mountains of Kilpisjarvi Host An Abundance of Threatened Plants in Finnish Lapland, Botanica Pacifica, 2, 43–52, https://doi.org/10.17581/bp.2013.02105, 2013.

Leppiniemi, O., Karjalainen, O., Aalto, J., Luoto, M., and Hjort, J.: Environmental spaces for palsas and peat plateaus are disappearing at a circumpolar scale, The Cryosphere, 17, 3157–3176, https://doi.org/10.5194/tc-17-3157-2023, 2023.

Leppänen, L., Kontu, A., Sjöblom, H., and Pulliainen, J.: Sodankylä manual snow survey program, Geoscientific Instrumentation, Methods and Data Systems, 5, 163–179, https://doi.org/10.5194/gi-5-163-2016, 2016.

Luoto, M., Heikkinen, R. K., and Carter, T. R.: Loss of palsa mires in Europe and biological consequences, https://doi.org/10.1017/S0376892904001018, 2004.

Lépy, E. and Pasanen, L.: Observed regional climate variability during the last 50 years in reindeer herding cooperatives of finnish Fell Lapland, Climate, 5, https://doi.org/10.3390/cli5040081, 2017.

Madani, N., Parazoo, N. C., and Miller, C. E.: Climate change is enforcing physiological changes in Arctic Ecosystems, Environmental Research Letters, 18, https://doi.org/10.1088/1748-9326/acde92, 2023.

Mandlburger, G. and Jutzi, B.: On the feasibility of water surface mapping with single photon lidar, ISPRS International Journal of Geo-Information, 8, https://doi.org/10.3390/ijgi8040188, 2019.

Markkula, I., Turunen, M., and Rasmus, S.: A review of climate change impacts on the ecosystem services in the Saami Homeland in Finland, https://doi.org/10.1016/j.scitotenv.2019.07.272, 2019.

Marti, R., Gascoin, S., Berthier, E., Pinel, M. D., Houet, T., and Laffly, D.: Mapping snow depth in open alpine terrain from stereo satellite imagery, The Cryosphere, 10, 1361–1380, https://doi.org/10.5194/tc-10-1361-2016, 2016.

Martin, L. C., Nitzbon, J., Scheer, J., Aas, K. S., Eiken, T., Langer, M., Filhol, S., Etzelmüller, B., and Westermann, S.: Lateral thermokarst patterns in permafrost peat plateaus in northern Norway, The Cryosphere, 15, 3423–3442, https://doi.org/10.5194/tc-15-3423-2021, 2021.

Meier, K.-D.: Permafrosthügel in Norwegisch und Schwedisch Lappland im Klimawandel, 2015.

Meloche, J., Langlois, A., Rutter, N., McLennan, D., Royer, A., Billecocq, P., and Ponomarenko, S.: High-resolution snow depth prediction using Random Forest algorithm with topographic parameters: A case study in the Greiner watershed, Nunavut, Hydrological Processes, 620   36, https://doi.org/10.1002/hyp.14546, 2022.

Meriö, L. J., Rauhala, A., Ala-Aho, P., Kuzmin, A., Korpelainen, P., Kumpula, T., Kløve, B., and Marttila, H.: Measuring the spatiotemporal variability in snow depth in subarctic environments using UASs - Part 2: Snow processes and snow-canopy interactions, The Cryosphere, 17, 4363–4380, https://doi.org/10.5194/tc-17-4363-2023, 2023.

Merkouriadi, I., Leppäranta, M., and Järvinen, O.: Interannual variability and trends in winter weather and snow conditions in Finnish 625   Lapland, Estonian Journal of Earth Sciences, 66, 47–57, https://doi.org/10.3176/earth.2017.03, 2017.

Michele, C. D., Avanzi, F., Passoni, D., Barzaghi, R., Pinto, L., Dosso, P., Ghezzi, A., Gianatti, R., and Vedova, G. D.: Using a fixed-wing UAS to map snow depth distribution: An evaluation at peak accumulation, The Cryosphere, 10, 511–522, https://doi.org/10.5194/tc-10-511-2016, 2016.

Nagelkerke, N. J. D.: A note on a general definition of the coefficient of determination, Biometrika, 78, 691–692, https://academic.oup.com/630   biomet/article/78/3/691/256225, 1991.

NOAA: March 2023 Global Snow and Ice Report, https://www.ncei.noaa.gov/access/monitoring/monthly-report/global-snow/202303, 2023.

Olaya, V.: Basic land-surface parameters, vol. 33, pp. 141–169, Elsevier Ltd, https://doi.org/10.1016/S0166-2481(08)00006-8, 2009.

Olaya, V. and Conrad, O.: Geomorphometry in SAGA, vol. 33, pp. 293–308, Elsevier Ltd, https://doi.org/10.1016/S0166-2481(08)00012-3, 2009.

635   Olvmo, M., Holmer, B., Thorsson, S., Reese, H., and Lindberg, F.: Sub-arctic palsa degradation and the role of climatic drivers in the largest coherent palsa mire complex in Sweden (Vissátvuopmi), 1955–2016, Scientific Reports, 10, https://doi.org/10.1038/s41598-020-65719-1, 2020.

Park, H., Fedorov, A. N., Zheleznyak, M. N., Konstantinov, P. Y., and Walsh, J. E.: Effect of snow cover on pan-Arctic permafrost thermal regimes, Climate Dynamics, 44, 2873–2895, https://doi.org/10.1007/s00382-014-2356-5, 2015.

640   Peng, X., Frauenfeld, O. W., Huang, Y., Chen, G., Wei, G., Li, X., Tian, W., Yang, G., Zhao, Y., and Mu, C.: The thermal effect of snow cover on ground surface temperature in the Northern Hemisphere, Environmental Research Letters, 19, https://doi.org/10.1088/1748-9326/ad30a5, 2024.

Probst, P., Wright, M. N., and Boulesteix, A. L.: Hyperparameters and tuning strategies for random forest, https://doi.org/10.1002/widm.1301, 2019.

645   Quante, L., Willner, S. N., Middelanis, R., and Levermann, A.: Regions of intensification of extreme snowfall under future warming, Scientific Reports, 11, https://doi.org/10.1038/s41598-021-95979-4, 2021.

Ran, Y., Li, X., Cheng, G., Che, J., Aalto, J., Karjalainen, O., Hjort, J., Luoto, M., Jin, H., Obu, J., Hori, M., Yu, Q., and Chang, X.: New high-resolution estimates of the permafrost thermal state and hydrothermal conditions over the Northern Hemisphere, Earth System Science Data, 14, 865–884, https://doi.org/10.5194/essd-14-865-2022, 2022.

650   Rauhala, A., Meriö, L. J., Kuzmin, A., Korpelainen, P., Ala-Aho, P., Kumpula, T., Kløve, B., and Marttila, H.: Measuring the spatiotemporal variability in snow depth in subarctic environments using UASs - Part 1: Measurements, processing, and accuracy assessment, The Cryosphere, 17, 4343–4362, https://doi.org/10.5194/tc-17-4343-2023, 2023.

Renette, C., Olvmo, M., Thorsson, S., Holmer, B., and Reese, H.: Multitemporal UAV lidar detects seasonal heave and subsidence on palsas, The Cryosphere, 18, 5465–5480, https://doi.org/10.5194/tc-18-5465-2024, 2024.

655 Revuelto, J., Billecocq, P., Tuzet, F., Cluzet, B., Lamare, M., Larue, F., and Dumont, M.: Random forests as a tool to understand the snow depth distribution and its evolution in mountain areas, Hydrological Processes, 34, 5384–5401, https://doi.org/10.1002/hyp.13951, 2020.

Revuelto, J., Alonso-Gonzalez, E., Vidaller-Gayan, I., Lacroix, E., Izagirre, E., Rodríguez-López, G., and López-Moreno, J. I.: Intercomparison of UAV platforms for mapping snow depth distribution in complex alpine terrain, Cold Regions Science and Technology, 190, https://doi.org/10.1016/j.coldregions.2021.103344, 2021.

660 Richiardi, C., Siniscalco, C., and Adamo, M.: Comparison of Three Different Random Forest Approaches to Retrieve Daily High-Resolution Snow Cover Maps from MODIS and Sentinel-2 in a Mountain Area, Gran Paradiso National Park (NW Alps), Remote Sensing, 15, https://doi.org/10.3390/rs15020343, 2023.

Seppälä, M.: An experimental study of the formation of palsas, https://www.researchgate.net/publication/255583596, 1982.

Seppälä, M.: Snow Depth Controls Palsa Growth, Permafrost and Periglacial Processes, 5, 283–288, 1994.

665 Seppälä, M.: An experimental climate change study of the effect of increasing snow cover on active layer formation of a palsa, Finnish Lapland, in: 8th Int. Conf. on Permafrost, edited by Phillips, M., Springman, S. M., and Arenson, L. U., pp. 1013–1016, Lisse: Swets Zeitlinger, ISBN 9058095827, 2003.

Seppälä, M.: Palsa mires in Finland, The Finnish environment, 23, 155–162, https://www.researchgate.net/publication/266241369, 2006.

Seppälä, M.: Synthesis of studies of palsa formation underlining the importance of local environmental and physical characteristics, Quater-
670 nary Research, 75, 366–370, https://doi.org/10.1016/j.yqres.2010.09.007, 2011.

Thackeray, C. W. and Fletcher, C. G.: Snow albedo feedback: Current knowledge, importance, outstanding issues and future directions, Progress in Physical Geography, 40, 392–408, https://doi.org/10.1177/0309133315620999, 2016.

Verdonen, M., Störmer, A., Lotsari, E., Korpelainen, P., Burkhard, B., Colpaert, A., and Kumpula, T.: Permafrost degradation at two monitored palsa mires in north-west Finland, The Cryosphere, 17, 1803–1819, https://doi.org/10.5194/tc-17-1803-2023, 2023.

675 Verdonen, M., Villoslada, M., Kolari, T., Tahvanainen, T., Korpelainen, P., Tarolli, P., and Kumpula, T.: Spatial distribution of thaw depth in palsas estimated from Optical Unoccupied Aerial Systems data, Permafrost and Periglacial Processes, 2024.

Walker, B., Wilcox, E. J., and Marsh, P.: Accuracy assessment of late winter snow depth mapping for tundra environments using structure-from-motion photogrammetry, Arctic Science, 7, 588–604, https://doi.org/10.1139/as-2020-0006, 2021.

Walser, H.: Statistik fu¨r Naturwissenschaftler, UTB, ISBN 9783825235413, 2011.

680 Wang, C., Shirley, I., Wielandt, S., Lamb, J., Uhlemann, S., Breen, A., Busey, R. C., Bolton, W. R., Hubbard, S., and Dafflon, B.: Local-scale heterogeneity of soil thermal dynamics and controlling factors in a discontinuous permafrost region, Environmental Research Letters, 19, https://doi.org/10.1088/1748-9326/ad27bb, 2024.

Willmott, C. J. and Matsuura, K.: Advantages of the mean absolute error (MAE) over the root mean square error (RMSE) in assessing average model performance, Climate Research, 30, 79–82, https://doi.org/10.2307/24869236, 2005.

685 Wilson, J. P. and Gallant, J. C.: Primary topographic attributes, pp. 51–85, https://www.researchgate.net/publication/303543730, 2000.

Wright, M. N. and Zigler, A.: ranger: A Fast Implementation of Random Forests for High Dimensional Data in C++ and R., Journal of Statistical Software, 77, 1–17, https://doi.org/10.18637/jss.v077.i01, 2017.

Yokoyama, R., Shlrasawa, M., and Pike, R. J.: Visualizing Topography by Openness: A New Application of Image Processing to Digital Elevation Models, Photogrammetic Engineering and Remote Sensing, 68, 257–265, 2002.

690 Zhang, K., Chen, S. C., Whitman, D., Shyu, M. L., Yan, J., and Zhang, C.: A progressive morphological filter for removing nonground measurements from airborne LIDAR data, IEEE Transactions on Geoscience and Remote Sensing, 41, 872–882, https://doi.org/10.1109/TGRS.2003.810682, 2003.

Zuidhoff, F. S.: Recent decay of a single palsa in relation to weather conditions between 1996 and 2000 in Laivadalen, northern Sweden, Geografiska Annaler, Series A: Physical Geography, 84, 103–111, https://doi.org/10.1111/1468-0459.00164, 2002.